Biophysical Journal Volume 71 December 1996 3454–3466

Theory, Design, and Characterization of a Microdialysis Flow Cell for Raman Spectroscopy

Roman Tuma and George J. Thomas, Jr.
Division of Cell Biology and Biophysics, School of Biological Sciences, University of Missouri—Kansas City, Kansas City, Missouri 64110 USA

ABSTRACT The theory, design, and application of a dialysis flow cell for Raman spectroscopy are described. The flow cell permits rapid collection of Raman spectra concurrent with the efflux of small solute molecules or ions into a solution of macromolecules and is well suited to acquisition of data during hydrogen-isotope exchange reactions of biological molecules. Kinetic parameters of the device are described by a diffusion model, which accounts satisfactorily for the observed rates of efflux of deuterium oxide ($k_{^2H} = 0.30\ min^{-1}$), calcium ions ($k_{Ca} = 0.10\ min^{-1}$) and EGTA ($k_{EGTA} = 0.07\ min^{-1}$). Application to the kinetics of glutamate protonation in a peptide copolymer [poly(Glu, Lys, Tyr)] shows that pH-titration rates as high as 3.3 pH units/min can be monitored. It is also shown that one can extract first-order hydrogen-isotope exchange rate constants from measured second-order exchanges by taking into account the rate of entry of ^2H_2O effluent into the bulk H_2O solution. Deuterium exchanges of the single-stranded polyribonucleotides poly(rA) and poly(rU) and of the double-stranded RNA genome from bacteriophage $\phi 6$ have been investigated. The measured nucleotide base exchange rates are comparable with those determined previously by other methods. The results indicate that base exchanges as fast as $\approx 2\ min^{-1}$ can be determined reliably with the present design. Application of the Raman flow cell to hydrogen-isotope exchange of the basic pancreatic trypsin inhibitor confirms consistency with results obtained previously on this protein by tritiation and NMR techniques.

INTRODUCTION

Elucidating the pathway of supramolecular assembly is an important problem in molecular biology but often represents a formidable challenge to the structural biologist. A frequently studied example is the formation of an icosahedral viral capsid from multiple copies of identical subunits. Typically, the viral morphogenetic pathway involves many steps, including the formation of transient intermediates, the folding of subunit domains that may participate in recognition, and the packaging of a viral genome (Teschke and King, 1993; Prevelige et al., 1993; Tuma et al., 1996a, b). The formation of a viral capsid also serves as a model for the construction of other architecturally complex cellular assemblies. Yet, the structural details and dynamic principles governing such assembly mechanisms remain largely unknown.

Understanding the molecular mechanism of capsid assembly requires the identification and characterization of structural intermediates along the assembly pathway. In principle, this task can be greatly facilitated by use of a time-resolved experimental approach. Because rapid changes in particle size or morphology can occur, the desired time resolution usually cannot be achieved with high-resolution structure methods, such as x-ray crystallography and multidimensional NMR. However, vibrational spectroscopy, in particular Raman spectroscopy, has the capability to provide insight into time-dependent changes in macromolecular conformation along such an assembly pathway. In addition to probing structural differences directly, Raman spectroscopy can be exploited as a probe of macromolecular dynamics. For example, the method is well suited to monitoring the kinetics of hydrogen-isotope exchange reactions involving labile protons of biological molecules. Raman spectroscopy can also be applied to samples of different morphology over wide ranges of experimental conditions. (For a recent review of related applications, see Miura and Thomas, 1995b.)

Factors that control macromolecular assembly in vivo include temperature, pH, ionic composition and ionic strength of solution, as well as the presence of nucleating and catalytic agents (Jacrot, 1975; Olkkonen et al., 1990; Orlova and Egelman, 1995). Protocols that allow these factors to be varied, singly or in combination, while Raman spectral data are collected simultaneously have been described by several investigators. For example, stop-flow methods in conjunction with resonance Raman spectroscopy have been employed to probe rapid kinetic processes (Hester, 1987). Alternatively, a microdialysis device has been incorporated within a Raman solution cell to effect the exchange of specific ions that trigger structural changes in the target molecules (Caillé et al., 1983). The latter methodology is suited to the investigation of relatively slow rates of exchange of the dialyzing agent (hereafter referred to as the effluent). It is also compatible with sample requirements for Raman spectroscopy, including optical homogeneity of the solution and relatively high solute concentration. In

Received for publication 29 July 1996 and in final form 10 September 1996.

Address reprint requests to Dr. George J. Thomas, Jr., Division of Cell Biology and Biophysics, School of Biological Sciences, University of Missouri-Kansas City, Kansas City, MO 64110. Tel.:816-235-5247; Fax: 816-235-5158; E-mail: thomasgj@cctr.umkc.edu.

0006-3495/96/12/3454/13 $2.00

recent applications the Raman microdialysis flow cell has been employed to characterize proton exchanges in protein subunits and packaged genomes of isometric viruses (Li et al., 1993; Reilly and Thomas, 1994; Tuma et al., 1996b)

To enhance the value of the Raman microdialysis approach for exchange experiments, an improved understanding of the method is required. Here, we present a simple diffusion model to establish quantitative correlations between design and performance of the microdialysis device. Applicability of the diffusion model is demonstrated by favorable comparison of calculated efflux rates with those measured on representative solutes. A framework for interpretation of hydrogen exchange experiments is developed and applied to protium–deuterium exchanges of model nucleic acid and protein molecules. The present results are compared with previously published studies of hydrogen exchanges in these biological molecules. The diffusion model is shown to provide a basis for continued refinements in the design and operation of the Raman microdialysis flow cell.

MATERIALS AND METHODS

A schematic diagram of the Raman microdialysis flow cell for use in the 90° laser scattering geometry is shown in Fig. 1. The sample solution is contained in a standard glass capillary of 1.0-mm internal diameter and ~2.0-cm length (Kimax #52034). A single fiber of SpectraPor (Spectrum, Inc., Houston, TX) hollow microdialysis tubing of 210-μm diameter and 6000 Da molecular-mass cutoff is also contained within the cell. During operation, the glass capillary is sealed at both ends with a generic rosin wax and the microdialysis tubing is attached by means of a modified pipette tip to a 10-ml syringe, which serves as the source of the dialyzing solution. Because of the low-molecular-mass cutoff of the microdialysis tubing, only small molecules (effluent) are transported across the permeable barrier. A constant flow of 2–3 ml/h, which is sufficient to maintain constant effluent concentration at the tubing boundary, is accomplished with a syringe injection pump (Harvard Instruments, South Natick, MA). The 1.0-mm capillary cell permits use of a standard Raman sample illuminator and thermostat jacket (Thomas and Barylski, 1970).

In the present research the Raman-scattered light was analyzed with a Spex model 1877 triple spectrograph (Spex Industries, Edison, NJ) equipped with a charge-coupled-device (CCD) array detector (model ST130, Princeton Instruments, Princeton, NJ). The CCD detector permits rapid acquisition of high-quality Raman data during solvent exchange reactions. Time resolution of the apparatus is approximately 30 s, which represents the minimum time typically required to collect a Raman spectrum of acceptable signal-to-noise ratio quality on aqueous biomolecules.

To determine the performance characteristics of the Raman dialysis flow cell we employed ^2H_2O effluent for deuterium exchange of the following H_2O solutions: polyethylene glycol (PEG) 8000, polyriboadenylic acid [poly(rA)], polyribouridylic acid [poly(rU)], double-stranded (ds) RNA from bacteriophage ϕ6, and bovine pancreatic trypsin inhibitor (BPTI). Additionally, effluxes of aqueous calcium nitrate [0.10 M $Ca(NO_3)_2$] and of the calcium chelator EGTA into pure H_2O were exam

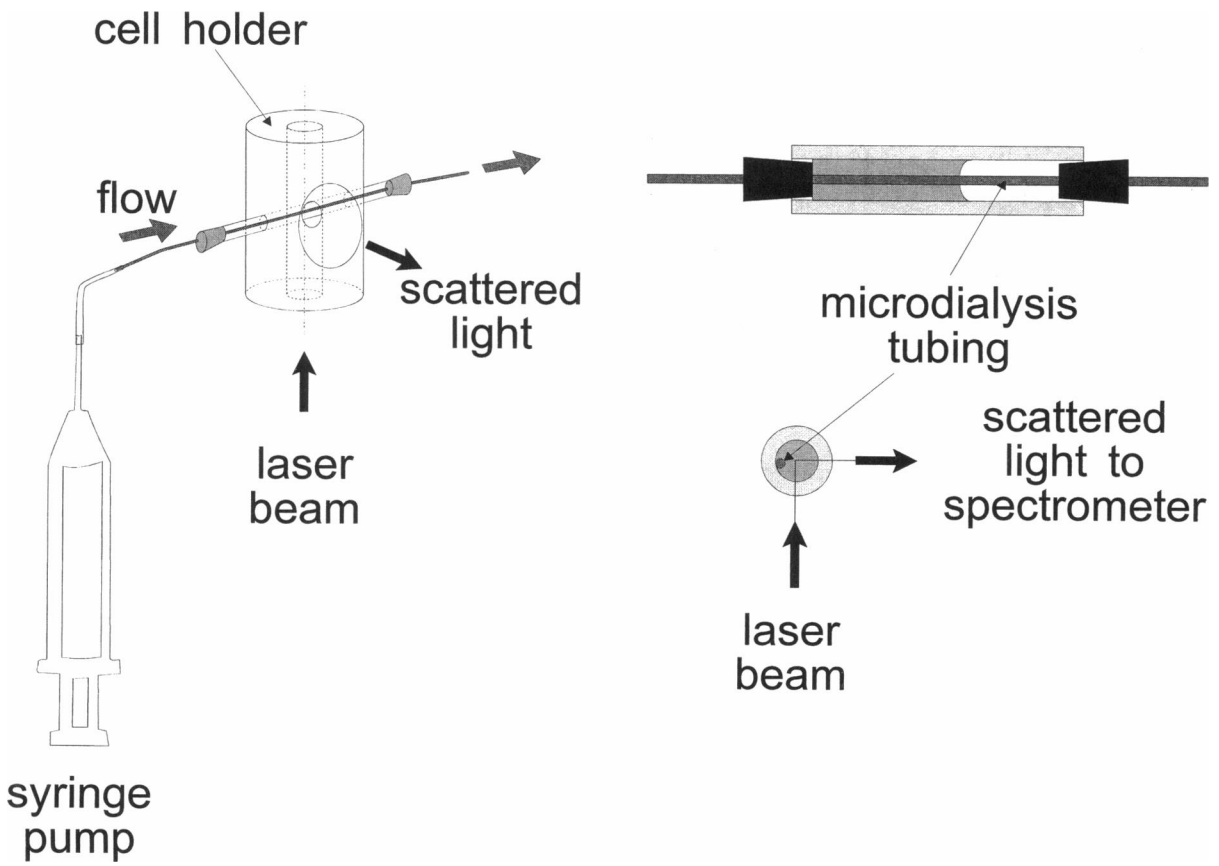

FIGURE 1 (*Left*) Frontal view showing the laser beam path, the thermostated sample cell holder, and the capillary sample cell in the 90° scattering geometry. (*Right*) Two sections through the capillary cell containing the sample solution (*light stippling*) and microdialysis tubing (*dark stippling*).

ined, Finally, protonation of glutamate carboxyls in the copolypeptide poly-L-(Glu, Lys, Tyr) was determined with HCl as the effluent. Reverse exchanges were also investigated. Further details of the experimental conditions are as follows.

Effluent solutions (H_2O or ^2H_2O) were introduced into 10% w/v solutions of PEG 8000 at 20°C at a 3-ml/h flow rate. The same conditions were used for 0.1 M $Ca(NO_3)_2$ solution (pH 5.5); the sodium salt of EGTA (0.2 M, pH 8) was delivered at 5 ml/h.

Solutions of the potassium salts of poly(rU) and poly(rA) (Sigma, St. Louis, MO) and of purified dsRNA from bacteriophage $\phi 6$ (gift of Prof. D. H. Bamford, University of Helsinki, Finland), each dissolved in 10 mM Tris-HCl (pH 7.4) at ≈40 mg/ml and thermostated at 10°C, were subjected to 10 mM Tris-^{2}HCl effluent (p^2H 7.4) at 3 ml/h.

The sodium salt of the peptide random copolymer poly-L-(Glu, Lys, Tyr), containing a 6:3:1 molar ratio of Glu:Lys:Tyr and an average molecular mass of 20–50 kDa (Sigma, lot #92H5536), was dissolved to 200 mg/ml in H_2O at pH 8.5 and 5°C and then subjected to 3.5 M HCl effluent (3 ml/h) to achieve a rapid decrease in pH.

BPTI (gift of Prof. C. Woodward, University of Minnesota, St. Paul) was dissolved to 70 mg/ml in 0.3 M KCl (pH 6.6) and exchanged at 10°C with 0.3 M KCl ^2H_2O (p^2H 6.6) effluent at 2 ml/h. We achieved complete deuterium exchange of peptide groups in BPTI by unfolding the protein dissolved at 9 mg/ml in 0.3 M potassium chloride–potassium deuteroxide solution (p^2H 13, 2 h at 25°C), followed by refolding in neutral solution (Hilton et al., 1981). The refolding reaction was started by adjustment of the p^2H to 6.5 with ^{2}HCl on ice. The refolded protein was filtered through a 0.2-μm microfuge filter and concentrated to 20 mg/ml for Raman spectroscopy.

THEORY

Numerical solution of the diffusion equation for small-molecule transport

Design of the Raman flow cell (Fig. 1) ensures that diffusion governs the transport of small molecules between the membrane boundary of the microdialysis tubing and the glass capillary containing the macromolecular solution. Thus, the solute concentration as a function of time $c(x, y, t)$ is determined by the diffusion equation (Eq. 1), which can be solved with appropriate boundary conditions, provided that the diffusion coefficient (D) is known for the solute species:

$$D\Delta c(x, y, t) = \partial c(x, y, t)/\partial t. \quad (1)$$

Because the length of the capillary cylinder is much greater than the cylinder's diameter, the solution of Eq. 1 is simplified to the planar scheme depicted in Fig. 2. We define a Cartesian coordinate system with the origin at the center of the capillary and the x axis bisecting the circular boundaries of both the glass capillary (Ψ_1) and the microdialysis tubing (Ψ_2). For Ψ_2 the boundary thickness (≈18 μm) is negligible compared with the path of diffusion (≈1 mm), and permeability to small molecules is very high. Accordingly, the solute concentration gradient across Ψ_2 can be ignored, and the Dirichlet boundary condition (Eq. 2) applies:

$$c(x, y, t) = c_0 : (x, y) \in \Psi_2, \quad (2)$$

where c_0 is the concentration of solute in the effluent solution. On the other hand, the glass capillary boundary Ψ_1 is impermeable, and the Neumann boundary condition (Eq. 3) must be applied:

$$\partial c(x, y, t)/\partial n = 0 : (x, y) \in \Psi_1, \quad (3)$$

where the derivative is with respect to the direction normal to the Ψ_1 boundary.

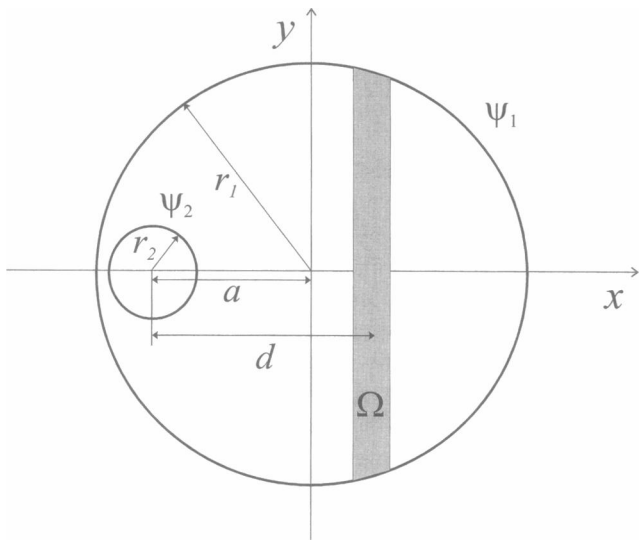

FIGURE 2 Cross-sectional view of a chamber representing diffusion of a low-molecular-weight solute from within a small cylindrical boundary (Ψ_2, microdialysis tubing) to a larger cylindrical boundary (Ψ_1, capillary sample cell). Typically, the radii r_1 of Ψ_1 and r_2 of Ψ_2 are 0.5 and 0.106 mm, respectively. The shaded area Ω (width ≈0.1 mm) is illuminated by the laser beam and provides the Raman signal. The distances between centers of the microdyalsis tubing and capillary cell and between centers of the microdialysis tubing and laser beam are labeled a (≈0.37 mm) and d, respectively. The origin of the Cartesian coordinate system used in the calculations coincides with the center of the capillary.

The boundary problems represented by Eqs. 1–3 can be solved numerically by use of the direct method on a square lattice with curved boundary conditions (Ozisik, 1980). The concentration profile $c(x, y, t)$ is integrated over the cross-section of sample exposed to the laser beam (Ω; see Fig. 2) to yield the average concentration of solute detected at time t. Thus,

$$c_s(t) = \iint_{(x,y)\in\Omega} c(x, y, t)\mathrm{d}x\mathrm{d}y = \frac{1}{n}\sum_{x_i, y_j \in \Omega} c(x_i, y_j, t), \quad (4)$$

where x_i and y_i are the lattice coordinates and n is the total number of lattice points in Ω.

Second-order kinetics of hydrogen exchange processes

In contrast to rapid (stop-flow) mixing methods, microdialysis diffusion takes place on a relatively long time scale, usually of the order of minutes. Therefore, it is necessary to take into account the true second-order character of kinetic processes involving the effluent (small molecule) and the

substrate (macromolecule). The same consideration applies to hydrogen-isotope exchanges effected by efflux of ^2H_2O solvent into H_2O solutions or vice versa. We employ the notation XH to denote a proton-exchangeable site in a target macromolecular species and X^2H as its deuteriated (deuteron-exchanged) counterpart. The corresponding solvent species (H_2O, ^2H_2O, HO^2H, OH^-, O^2H^-, H^+, and $^2H^+$) are accounted for in the total protium [H] and deuterium [^{2}H] concentrations. The second-order rate for the exchange reaction, $XH + {}^2H \rightleftarrows {}^2HX + H$, is given by

$$d[XH]/dt = -k_f^{(2)}[XH][^2H] + k_r^{(2)}[X^2H][H], \qquad (5)$$

where $k_f^{(2)}$ and $k_r^{(2)}$ are, respectively, the forward and the reverse second-order rate constants. If we define $\Phi_d(t)$ and $\Phi_h(t)$ as the respective time-dependent mole fractions of deuteriated and protiated solvent species, and $\Theta_d = [X^2H]/([XH]+[X^2H])$ and $\Theta_h = [XH]/([XH]+[X^2H])$ as the mole fractions of deuteriated and protiated target species, then Eq. 5 can be rewritten as follows:

$$d\Theta_h/dt = -k_f^{(2)}[XH][^2H]_\infty\Phi_d + k_r^{(2)}[X^2H][H]_0\Phi_h, \qquad (6)$$

where the subscripts 0 and ∞ indicate the initial and final concentrations, respectively. The second-order rate constants are related to pseudo-first-order rate constants (as measured, for example, by rapid mixing methods) as follows:

$$k_f = k_f^{(2)}[^2H]_\infty, \qquad k_r = k_r^{(2)}[H]_0. \qquad (7)$$

Using $\Theta_d = 1 - \Theta_h$ and Eq. 7, we obtain from Eq. 6

$$d\Theta_h/dt = -k_f\Theta_h + (k_f - k_r)\Phi_h\Theta_h + k_r\Phi_h. \qquad (8)$$

The rate constants k_f and k_r, which represent exchange rates in ^2H_2O and H_2O, respectively, have been shown to be approximately equal, owing to compensation of kinetic isotope effects (Englander et al., 1979; Englander and Kallenbach, 1984; Connelly et al., 1993). Thus, Eq. 8 reduces to

$$d\Theta_h/dt = -k_f\Theta_h + k_r\Phi_h. \qquad (9)$$

Equation 9 yields the first-order rate constant when both Θ_h and Φ_h are determined experimentally to high accuracy. A formally identical equation is obtained for $d\Theta_d/dt$ on interchanging indices h and d. When Θ_h and Φ_h are subject to significant experimental errors, Eq. 9 is less useful than its integrated form. By analogy with the general solution to the diffusion equation (Ozisik, 1980), the time-dependent fractions of deuteriated and protiated species sampled by the laser beam are approximated as

$$\Phi_d(t) = 1 - e^{-k_d t}, \qquad \Phi_h(t) = e^{-k_d t}. \qquad (10)$$

The solution to Eq. 9 with the initial condition $\Theta_h(0) = 1$ is then given by

$$\Theta_h(t) = (k_f e^{-k_d t} - k_d e^{-k_d t})/k_f - k_d \qquad \text{for } k_f \neq k_d, \qquad (11a)$$

$$\Theta_h(t) = (k_f t + 1)e^{-k_f t} \qquad \text{for } k_f = k_d. \qquad (11b)$$

The fraction of deuteriated sites, $\Theta_d = 1 - \Theta_h$, is also obtained directly from Eq. 11.

RESULTS AND DISCUSSION

Diffusion model

To test the applicability of the diffusion model to the system described by Fig. 2 we measured the efflux of Ca^{2+} ions (calcium nitrate solution) into H_2O. This process is easily monitored spectroscopically because the NO_3^- counterions generate a distinctive Raman marker at 1050 cm^{-1}. The experimental results were compared with those predicted from Eqs. 1–3, assuming a Ca^{2+} ion translational diffusion coefficient of 1.2×10^{-5} cm^2/s (Weast and Selby, 1966). The calculated results are presented in Fig. 3, which displays graphically the predicted distribution of Ca^{2+} effluent in the Ψ_1 domain before diffusion (0 min) and following diffusion periods of 2, 10, and 20 min. Essentially complete equilibration of the effluent is achieved after 20 min. Interestingly, for the off-center configuration of the microdialysis tubing the predicted concentration profile is nearly independent of the y coordinate in the area (Ω) sampled by the laser beam. Therefore, no significant concentration gradient is expected within Ω. Fig. 4 displays the time-dependent Ca^{2+} concentration within Ω, as determined by Eq. 4 for different values of d (distance along x between the centers of the microdialysis tubing and Ω). The theoretical curve is well approximated in each case by a single exponential term, except when $d < 0.3$ mm. The dependence of the apparent Ca^{2+} efflux rate on d is plotted in the inset of Fig. 4, which reveals that the rate decreases only slightly ($\leq$10%) with increasing d. For $d = 0.22$ mm the inadequacy of the single exponential approximation is apparent from Fig. 4.

Apart from the dependence of efflux rate on laser beam location, we have also examined the effects of capillary and microdialysis tubing radii. Calculated rates of Ca^{2+} efflux for several representative configurations are listed in Table 1. Increasing the capillary size (Ψ_1) clearly increases the time required to reach equilibrium, whereas increasing the microdialysis tubing size (Ψ_2) has the reverse effect. The values of r_2 included in Table 1 represent the nominal radii of dry (0.11 mm) and wet (0.12 mm) microdialysis tubing. The theoretical efflux rate of calcium was calculated to be 0.11 min^{-1}.

We can obtain a solution to the boundary problem (Eqs. 1–3) for different values of the diffusion coefficient by rescaling the time coordinate ($t' = Dt$). Thus, for the typical experimental geometry ($r_1 = 0.5$, $r_2 = 0.12$, and $a = 0.35$ mm), the solute efflux rate (k_s) can be calculated from Eq. 12:

$$k_s = 9167D_s, \qquad (12)$$

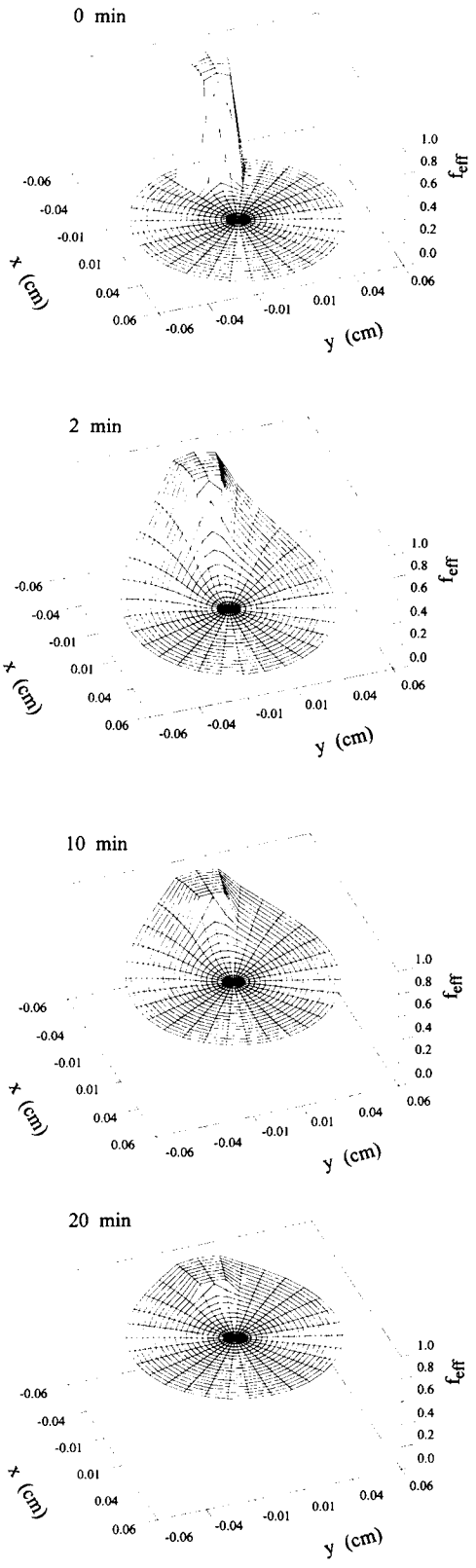

FIGURE 3 Graphical representation of time-dependent solutions of the diffusion equation (Eq. 1) for calcium nitrate in the planar x, y-coordinate system of Fig. 2 after efflux times t = 0, 2, 10, 20 min. The z axis of each plot shows the relative effluent concentration, $f_{eff}(t) = [Ca(NO_3)_2]_t/[Ca(NO_3)_2]_\infty$, at the indicated time.

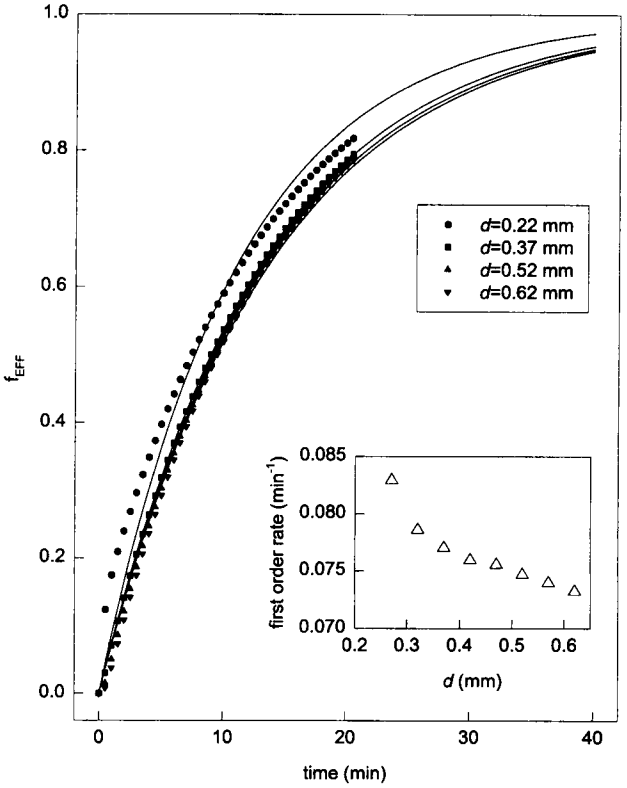

FIGURE 4 Calculated concentration of calcium nitrate effluent, f_{eff}, for different values of the parameter d (Fig. 2). (*Solid curves*) Least-squares single exponential fits used to determine the apparent efflux rates (Table 2). (*Inset*) Dependence of the efflux rate on d for the case a = 0.37 mm, as calculated by Eq. 4 using data from Fig. 3.

with k_s in min^{-1} and D_s in cm^2/s. For other experimental configurations a different numerical factor will appear in Eq. 12.

Experimental determination of efflux rates for small solutes

To compare the above theoretical results with experiment, the following time-dependent diffusion processes were monitored in the microdialysis flow cell by Raman spectroscopy: 1) efflux of H_2O into a 10% (w/v) solution of PEG in ^2H_2O, 2) efflux of ^2H_2O into a 10% (w/v) solution of PEG in H_2O, 3) efflux of 0.1 M $Ca(NO_3)_2$ into H_2O, and 4) efflux of EGTA into H_2O. The results, shown graphically in

TABLE 1 Dependence of the rate of calcium efflux on flow cell dimensions

r_1 (mm)	r_2 (mm)	k_{Ca} (min^{-1})
0.5	0.11	0.07
0.5	0.12	0.11
1.5	0.11	0.02

The flow cell parameters r_1 and r_2 are defined in Fig. 2. The rate constant for efflux of Ca^{2+}, k_{Ca}, was calculated with Eqs. 1–4, as described in the text.

Fig. 5, yielded the following first-order rates: $k_H = 0.48 \pm 0.01\ min^{-1}$, $k_{^2H} = 0.287 \pm 0.005\ min^{-1}$, $k_{Ca} = 0.10 \pm 0.01\ min^{-1}$, and $k_{EGTA} = 0.07 \pm 0.01\ min^{-1}$. Each rate constant represents a single exponential fit to the corresponding data set in Fig. 5. Interestingly, the experimental rates are in excellent agreement with the theoretical values predicted for wet microdialysis tubing and slightly higher than the values predicted for dry tubing. The corresponding rates calculated from available diffusion coefficients by use of Eq. 12 are listed with the experimental values in Table 2. (Although no published diffusion coefficient could be found for EGTA, the present measurement in combination with Eq. 12 suggests the value $D_{EGTA} = 0.76 \pm 0.01 \times 10^{-5}\ cm^2/s$).

Table 2 indicates that the diffusion model satisfactorily explains the efflux of isotopic solvent species and low-molecular-weight solutes in the flow cell assembly of Fig. 2. Table 1 suggests further that the diffusion characteristics of larger microdialysis tubing, larger sample cells, or both can be discriminated experimentally. The consistency between experimental and theoretical results implies further that precise positioning of the laser beam within the sample cell is not a source of significant experimental error.

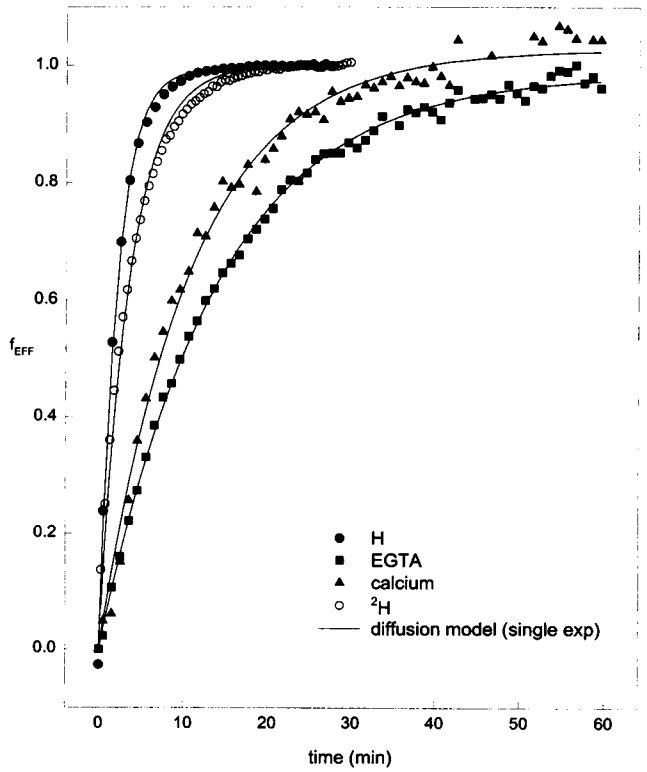

FIGURE 5 Raman measurement of the efflux of low-molecular-weight species in the microdialysis flow cell of Fig. 1. The calcium nitrate concentration was determined from the intensity of the Raman band of NO_3^- at 1050 cm^{-1}, the EGTA concentration from the intensity of the Raman band of CO_2^- at 1405 cm^{-1}, and the protium and the deuterium concentrations from the integrated intensities of their respective solvent Raman bands at 3000–3600 and 2300–2800 cm^{-1}. Intensities for $Ca(NO_3)_2$ and EGTA were normalized with respect to the H_2O band at 1635 cm^{-1}; intensities for H and ^2H efflux were normalized by use of the bands at 2700–2950 cm^{-1} from 10% polyethylene glycol added as an internal standard (Li, 1992).

TABLE 2 Comparison of calculated and experimental efflux rate constants

Effluent	D (cm^2/s)	k_{calc} (min^{-1})	k_{exp} (min^{-1})
H_2O	5.0×10^{-5}	0.46	0.48 ± 0.01
^2H_2O	3.0×10^{-5}	0.28	0.29 ± 0.01
$Ca(NO_3)_2$	1.2×10^{-5}	0.11	0.10 ± 0.01

The diffusion constant D for each effluent at 20°C is from Weast and Selby (1966). Calculated rates k_{calc} are from Eqs. 1–4, as described in the text.

The dependence of the calculated efflux rates on the geometry of the system (Table 1) suggests two ways to improve the time resolution of the flow cell of Fig. 2. First, a decrease in the sample cell radius (r_1) would reduce the mean path of molecular diffusion; second, an increase in the microdialysis tubing radius (r_2) would enlarge the effective permeable surface. In principle, both improvements could be realized by a semicylindrical sample cell with r_1 only slightly larger than the laser beam diameter ($\approx$150 μm) and with the flat face consisting of a dialysis membrane. Although such a design results in a 10-fold increase in the calculated rate of diffusion, it invalidates the single exponential approximation and would complicate the data analysis.

Application to biological macromolecules

Rate of titration of a glutamate-containing polypeptide, poly-L-(Glu, Lys, Tyr)

To apply the microdialysis flow cell to a biopolymer titration we have resolved the pH titration of glutamic acid side chains in the peptide random copolymer poly-L-(Glu, Lys, Tyr), with a Glu:Lys:Tyr molar ratio of 6:3:1. Raman markers specific to the CO_2^- and COOH ionization states of the glutamate sidechains provide a convenient basis for monitoring the time dependence of protonation of CO_2^- with decreasing pH. Additionally, the interspersed lysine and tyrosine residues of the copolymer effectively eliminate cooperativity in the pH-induced coil $\rightarrow$ α-helix conformational transition of this polypeptide and improve solubility of the low-pH form. The relatively strong Raman bands of Tyr provide as well a convenient and reliable internal intensity standard.

Raman spectra of high- and low-pH forms of poly-L-(Glu, Lys, Tyr) are shown in the upper panel of Fig. 6. The Raman marker of the CO_2^- group (symmetric O—C—O stretching vibration) occurs at 1408 cm^{-1}. Conversely, the COOH state is marked by the broad band at 1712 cm^{-1} (C=O stretching vibration; Lord and Yu, 1970). We used the normalized peak heights of both bands to measure the degree of carboxyl protonation as a function of time of H^+ efflux. As a consequence of protonation, the polymer undergoes a structural transition from random coil, represented by Raman amide I and III signatures at 1660 and

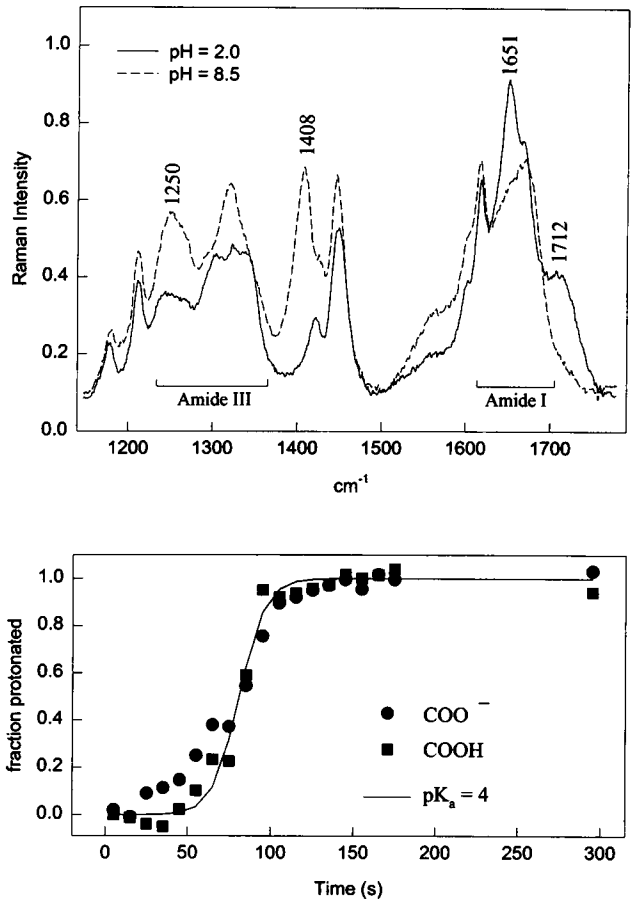

FIGURE 6 (*Top*) Raman spectra of acidic (pH 2) and basic (pH 8.5) forms of poly-L-(Glu, Lys, Tyr). Labels indicate marker bands discussed in the text. (*Bottom*) Time dependence of poly-L-(Glu, Lys, Tyr) protonation induced by 3.5 M HCl effluent. The fractions of protonated and ionized glutamates were calculated from the intensities of the 1730- and 1405-cm^{-1} bands, respectively, with the tyrosine band at 642 cm^{-1} used as an internal standard.

1250 cm^{-1}, respectively, to an α-helical conformation, represented by a strong and sharp Raman amide I band at 1650 cm^{-1} (Koenig and Frushour, 1972). As expected, the α-helix conformation also contributes amide III bands at 1270, 1300, and 1344 cm^{-1} (Bandekar, 1992).

The time course of protonation of poly-L-(Glu, Lys, Tyr) with H^+ efflux (3.5 M HCl) is shown in the lower panel of Fig. 6. The attendant conformational change, as reflected in amide I, is generally slower than protonation, presumably because of the effect of solution viscosity on polypeptide chain rearrangements. Thus, we can assume that titration of the glutamate sidechains in random coil poly-L-(Glu, Lys, Tyr) approximates the titration of free glutamic acid, for which $pK_a \approx 4$. Theoretical calculations indicate that the time course of H^+ efflux follows Eq. 10, which suggests an approximately linear correspondence between time and pH:

$$pH(t) = pH_0 - k_{pH}t, \tag{13}$$

where k_{pH} is the rate of pH change and pH_0 (= 8.5) represents the initial solution pH. When Eq. 13 is employed in a simple titration equilibrium, the fraction of protonated glutamate sidechains (χ_H) at time t is given by

$$\chi_H = 10^{-k_{pH}t}/(10^{-pK_a} + 10^{-k_{pH}t}). \tag{14}$$

Fig. 6 (bottom) shows that when $pK_a = 4.0$ the best fit of the experimental data to Eq. 14 yields $k_{pH} = 3.3 \pm 0.1$ min^{-1}. The computation of k_{pH} from Eq. 14 is not highly sensitive to the value of pK_a within ± 1 unit or so. For example, with $pK_a = 5$ (3), k_{pH} becomes 2.6 (4.0) min^{-1}. Conformational and electrostatic effects in poly-L-(Glu, Lys, Tyr) are not expected to alter the glutamate pK_a by more than one unit. We conclude that the rate of pH change is 3.3 ± 0.1 min^{-1}, which is fast enough to permit time resolution of biologically important processes governed by glutamate or aspartate protonation. An interesting example is the capsid conformational change associated with pH-induced expansion of cowpea chlorotic mottle virus (Jacrot, 1975; Speir et al., 1995).

Hydrogen-isotope exchange of ribonucleic acids

Poly(rA). Fig. 7 illustrates Raman spectra obtained during real-time deuterium exchange of poly(rA). The growth of a prominent band at 1205 cm^{-1} (^2H_2O bending mode) and the concomitant decay of the prominent band at 1635 cm^{-1} (H_2O bending) indicate solvent exchange. Additionally, the transient band at 1450 cm^{-1} (^2HOH bending) is discernible in the spectra. All other bands are assignable to either the adenine base or the ribose-phosphate backbone. Two prominent backbone markers appear at 810 and 1100 cm^{-1} and are assigned to O—P—O phosphodiester and PO_2^- phosphodioxy stretching vibrations (Thomas and Tsuboi, 1993). Both bands are insensitive to isotopic exchange of adenine and ribose and can be exploited as internal intensity standards. The frequency and intensity of the 810-cm^{-1} band implies that ~80% of the backbone assumes the A-type conformation (Thomas and Hartman, 1973). Shoulders at 790 and 822 cm^{-1} may represent lesser amounts of other phosphodiester conformations. The nucleosides of poly(rA) assume the C3′-*endo*/*anti* conformation, as judged by the occurrence of a 644-cm^{-1} marker and the absence of a 665-cm^{-1} marker (Benevides et al., 1986).

Many Raman bands in the poly(rA) spectrum are sensitive to base and ribose deuteriations. For example, the $N6H_2 \rightarrow N6^2H_2$ exchange leads to a frequency shift of the adenine ring breathing mode from 725 to 719 cm^{-1}. Therefore, the normalized intensity of the 719-cm^{-1} band can be used to monitor the fraction of adenine bases deuteriated at the $N6H_2$ position. In the top panel of Fig. 8 the progress of adenine deuteriation (represented by the growth of the 719 cm^{-1} marker) is compared with the progress of deuterium efflux (measured by the intensity of the 1205-cm^{-1} band). Clearly, adenine $N6H_2$ deuteriation lags behind deuterium efflux. Application of the second-order rate treatment (Eq. 9 or 11a) yields a true first-order rate of 1.5 ± 0.1 min^{-1}. An identical rate is obtained by use of the adenine ring modes

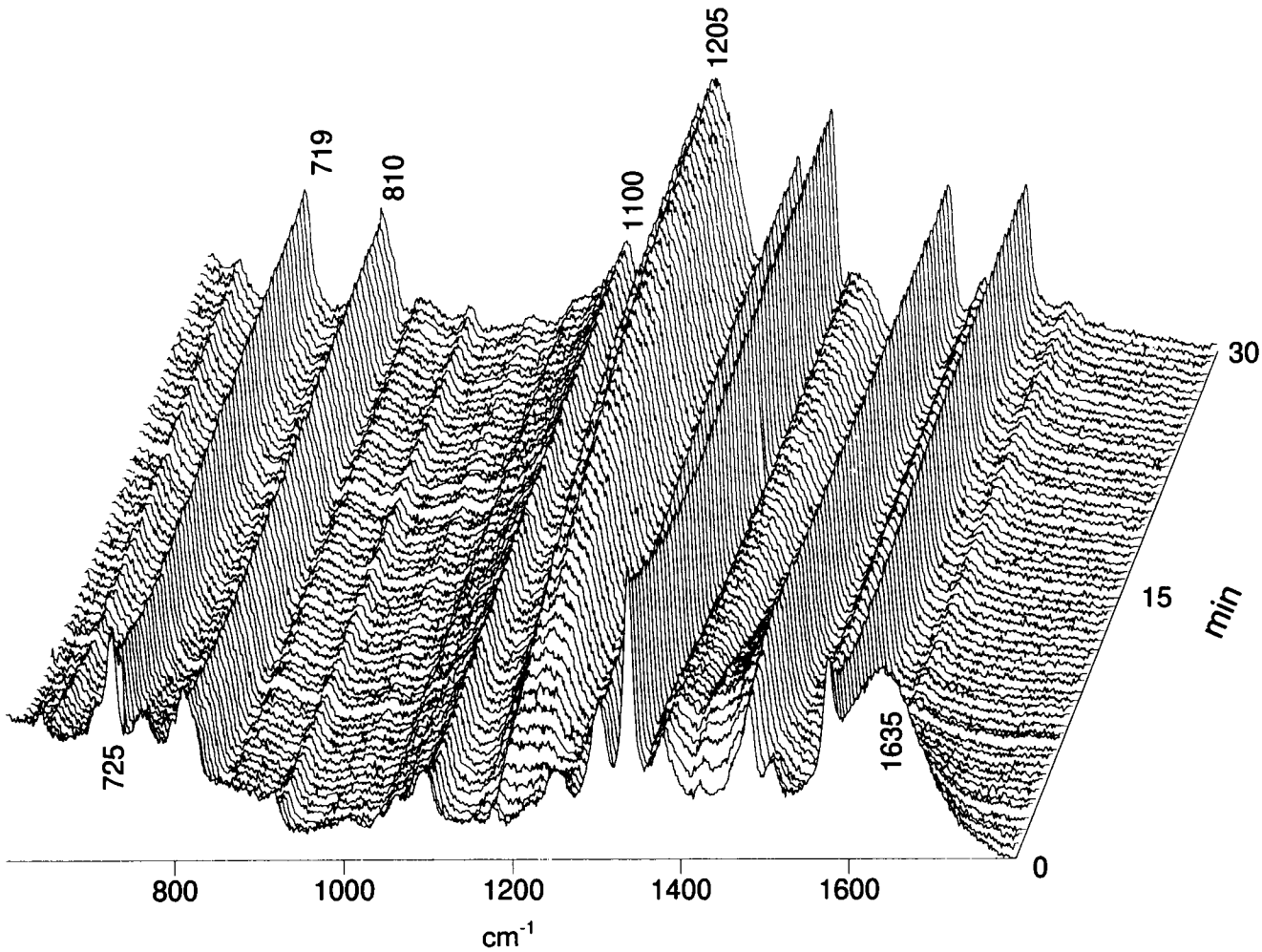

FIGURE 7 Raman spectra (600–1800 cm^{-1}) of poly(rA), initially dissolved at 40 mg/ml in 10 mM Tris-H_2O solution, as a function of time of exposure to Tris-^2H_2O effluent. Each spectrum was acquired in 30 s. Other experimental conditions are described in the text.

at 1337 cm^{-1} ($N6H_2$ form) and at 1342 cm^{-1} ($N6^2H_2$ form). Previous studies have shown that the amino proton exchange rate for the adenine mononucleotide rAMP is ~180 min^{-1} at 20°C or 60 min^{-1} at present conditions (10°C) (Mandal et al., 1979). As noted by Mandal et al. (1979), the exchange rate of adenosine polynucleotides decreases with increasing conformational order, presumably because of base-stacking interactions. Our results may therefore be interpreted as reflecting a high degree of base stacking in poly(rA) at 10°C. In fact, the currently determined poly(rA) exchange rate (1.5 min^{-1}) is similar to that reported for the poly(rA)·poly(rU) duplex (3 min^{-1}; Mandal et al., 1979). The present application of the microdialysis flow cell to poly(rA) exchange also demonstrates that a true first-order rate can be extracted from a second-order exchange process.

Poly(rU). To assess the limiting rate that can be measured with the present apparatus, we examined the rapid imino proton (N3H) exchange of poly(rU). The progress of uracil N3H deuteriation was monitored by the shift of the 782-cm^{-1} band to 773 cm^{-1} (Li et al., 1993) and is illustrated in the bottom panel of Fig. 8. Clearly, the N3H → $N3^2H$ exchange follows closely the efflux of ^2H_2O. This differs from the case of adenine N6 amino exchange (Fig. 8, upper panel) and is as expected for the fast imino proton exchange of poly(rU) for which $k_{ex} \approx 1000$ min^{-1} (Mandal et al., 1979). Decomposition of the poly(rU) second-order exchange process, as described above for poly(rA), yielded an apparent N3H → $N3^2H$ exchange rate between 10 and 100 min^{-1}. For comparison, the curve corresponding to a second-order exchange rate constant of 2 min^{-1} is also shown in the lower panel of Fig. 8. This curve is at the very limit (standard error deviation) of the experimental data and thus suggests that a rate of 2 min^{-1} is the limiting rate that could be resolved by the present system. Nevertheless, the above applications to poly(rA) and poly(rU) demonstrate that the present system can be implemented to distinguish qualitatively between fast ($k > 2$ min^{-1}) and slow ($k < 2$ min^{-1}) exchanges in nucleic acids and that the latter rates can be measured with quantitative precision.

ϕ6 dsRNA. Fig. 9 compares the Raman spectrum of genomic double-stranded (ds) RNA of bacteriophage ϕ6,

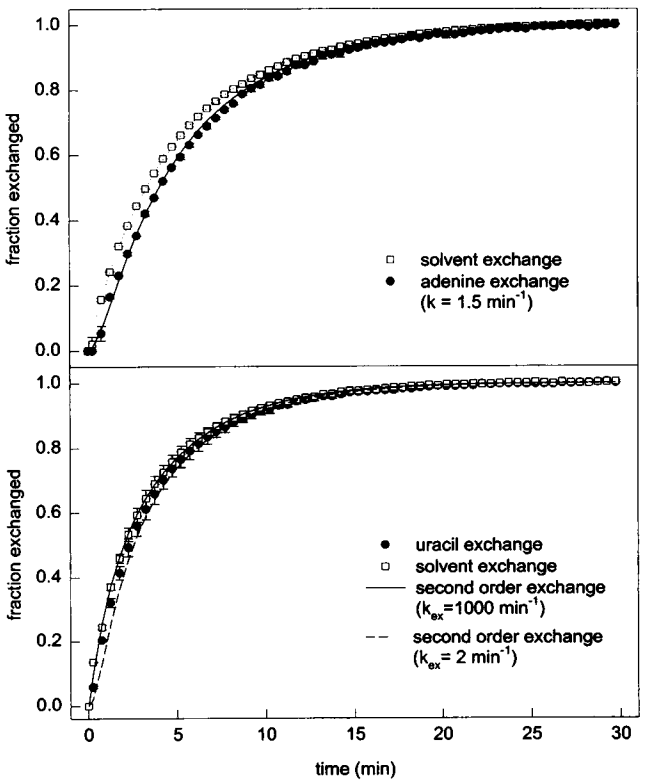

FIGURE 8 *Top*: The time course of adenine amino proton exchange in poly(rA) monitored by the intensity of the 719-cm^{-1} band of N6-deuteriated adenine. The solid line represents a second-order fit of the data using Eq. 11. *Bottom*: The time course of uracil imino proton exchange in poly(rU) monitored by the intensity of the 774 cm^{-1} band of N3-deuteriated uracil. The solid and dashed lines represent the exchange profiles calculated by Eq. 11 with k_f = 1000 and k_f =2 min^{-1}, respectively. The dotted curve in each panel represents the measured solvent efflux.

collected after 60 min of incubation in ^2H_2O buffer at p^{2}H = 7.6 (top), with the corresponding H_2O solution spectrum (middle). The Raman intensity ratio of bands at 813 and 1100 cm^{-1} in the H_2O solution spectrum, I_{813}/I_{1100}, has the value 1.6, which is indicative of a fully ordered *A* RNA conformation (Thomas and Hartman, 1973; Bamford et al., 1993). C3′-*endo*/*anti* nucleoside conformations are also evident from marker bands of the 600–800-cm^{-1} region (Thomas and Tsuboi, 1993). The ϕ6 genome serves as a good model for double-stranded RNA of nonuniform base sequence.

The digital difference spectrum of Fig. 9 (bottom) reveals a pattern of peaks and troughs, most of which result from shifts of band maxima attendant with deuteriation of base amino and imino sites and ribose C2′ hydroxyls. The time-dependent change in difference band intensities can be employed to monitor the RNA exchanges in real time.

We consider first the exchange of guanine residues, which can be monitored by use of either two guanine markers, viz., bands at 670 and 1716 cm^{-1} (Miura and Thomas, 1995a). From the time-dependent change of the 670-cm^{-1} band an apparent exchange rate of 0.8 ± 0.1 min^{-1} is obtained (Fig. 10). Presumably, this corresponds to the guanine amino exchange reaction ($N2H_2 \rightarrow N2^2H_2$), which is expected to be much slower than the guanine imino exchange ($N1H \rightarrow N1^2H$). (See the discussion of poly(rA) and poly(rU), above.) Similarly, the rate calculated from the time-dependent intensity change of the 1716-cm^{-1} band is 1.2 ± 0.2 min^{-1} (Fig. 10). The slightly higher rate computed from the 1716-cm^{-1} band presumably reflects the greater sensitivity of this band to competing imino exchange (Miura and Thomas, 1995a). Nonetheless, the rate measured here for guanine amino exchange in a Watson–Crick RNA duplex is an order of magnitude faster than reported previously [0.16 min^{-1} in poly(rG)·poly(rC) reported by Teitelbaum and Englander (1975)]. The more rapid guanine exchange in ϕ6 dsRNA may reflect the random distribution of G·C basepairs within the viral genome, which perhaps facilitates transient basepair openings.

The rate of exchange of adenine in dsRNA was estimated from the time-dependent shift of intensity of the adenine mode from 724 to 716 cm^{-1} (Figs. 9 and 10). The measured rate of 0.8 ± 0.1 min^{-1} is identical to that of guanine and reflects similar mechanisms of exchange for the two purines (Teitelbaum and Englander, 1975; Englander and Kallenbach, 1984). It is interesting to note that analysis of the 1482-cm^{-1} imidazole ring mode of adenine and guanine also yields essentially the same rate constant (data not shown).

The band at 784 cm^{-1} is due primarily to uracil (ring breathing mode), with a lesser contribution from the similar mode of cytosine. On deuteriation of dsRNA, the band shifts to 776 cm^{-1} (Fig. 9), reflecting uracil $N3H \rightarrow N3^2H$ and cytosine $N4H_2 \rightarrow N4^2H_2$ exchanges. We have exploited this shift to measure the apparent rate constant for pyrimidine ring exchanges. As shown by Fig. 10, the progress of pyrimidine exchange is nearly as rapid as deuterium efflux, yielding the apparent rate of 2.2 ± 0.3 min^{-1}. This is close to the time-resolution limit of the method and evidently reflects the rapid exchange of both uracil and cytosine protons (Guéron and Leroy, 1992). It should be noted that, at present conditions (p^{2}H = 7.4), the cytosine amino exchange is accelerated by specific base (O^2H^-) catalysis (Teitelbaum and Englander, 1975; Englander and Kallenbach, 1984). Accordingly, the same rate is obtained from the time-dependent shift of the 630-cm^{-1} cytosine marker to 620 cm^{-1} (data not shown).

RNA structures typically exhibit a Raman band at 919 cm^{-1}, assignable to C—O and C—C stretching of ribose (J. M. Benevides, M. Tsuboi, and G. J. Thomas, Jr., unpublished results). The band shifts to 910 cm^{-1} on deuteriation of the C2′ hydroxyl. The kinetics of $C2'OH \rightarrow C2'O^2H$ exchange, monitored by the intensity at 910 cm^{-1}, is indistinguishable from deuterium efflux (Fig. 10), indicating that $k_{C2'OH} > 2$ min^{-1}. The rapid C2′OH exchange reflects the low pK_a value that governs hydroxyl ionization as well as the solvent exposure of C2′ hydroxyls in the *A* RNA struc

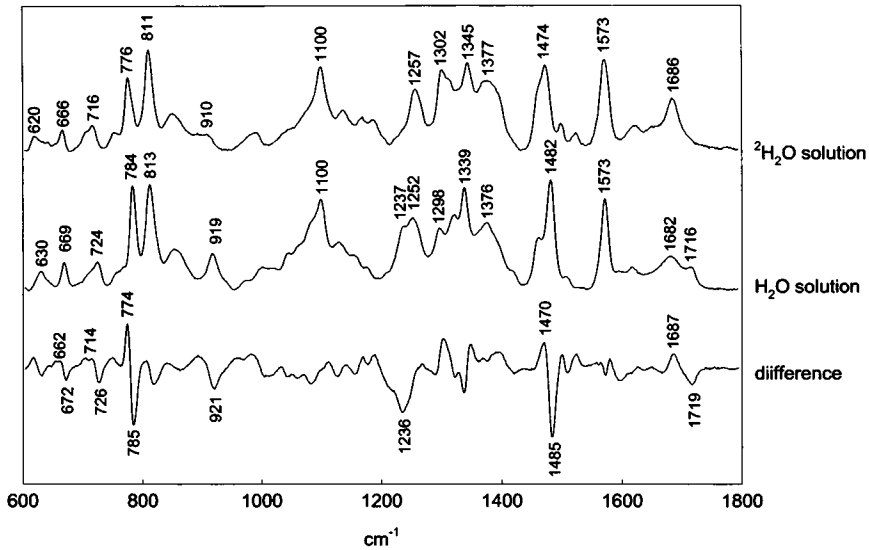

FIGURE 9 Raman spectra (600–1800 cm^{-1}) of deuteriated (*top trace*) and protiated (*middle trace*) forms of ϕ6 dsRNA, and their difference spectrum (*bottom trace*). The top spectrum was collected after 60 min in ^2H_2O. Labels in the difference spectrum indicate prominent bands that are employed to monitor hydrogen-isotope exchange, as discussed in the text.

ture (Saenger, 1984). Similar rapid exchange is expected for exposed hydroxyls of serine, threonine, and tyrosine side chains in proteins.

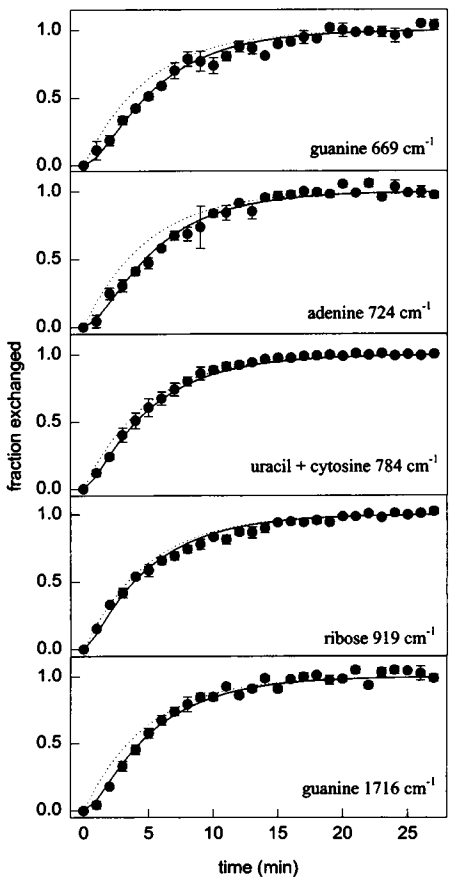

FIGURE 10 Hydrogen-isotope exchange of dsRNA bases and sugar moieties monitored by several deuteriation-sensitive Raman bands, as indicated. In each panel the dotted curve represents the efflux of solvent (^2H_2O) and the solid curve gives the least-squares second-order fit to the data (●).

In summary, the microdialysis flow cell of Fig. 2 is effective in monitoring exchange reactions of nucleic acids with rates of 2 min^{-1} or less. In practice this permits straightforward measurement of most amino proton exchanges of purine and pyrimidine nucleotides in DNA and RNA structures. Imino exchanges, although they are not generally accessible, can be monitored kinetically when specific protection is afforded by secondary, tertiary, or quaternary structures, as in the cases of *Z* DNA, tRNA, or quadruplexes of guanine or cytosine (Miura and Thomas, 1995a; Guéron and Leroy, 1992).

Exchange of bovine pancreatic trypsin inhibitor

Fig. 11 compares Raman spectra of BPTI in H_2O solution (*bottom trace*), in ^2H_2O solution after 180-min exposure to deuterium oxide (*middle trace*), and in ^2H_2O solution after complete deuteriation achieved by unfolding and refolding in a ^2H_2O environment (*top trace*). The bottom spectrum exhibits amide I and amide III bands centered at 1665 and 1244 cm^{-1}, respectively, indicating β-strand and irregular peptide chain conformations (Miura and Thomas, 1995b) consistent with the crystal structure (Wlodawer et al., 1987). The strong band at 1004 cm^{-1} in all spectra is due to the phenylalanine residues of BPTI and serves as a convenient internal intensity standard. (Complete assignments will be reported elsewhere and are available on request.)

The amide I peak at 1665 cm^{-1} shifts to 1655 cm^{-1} (amide I′) on full deuteriation of BPTI achieved by unfolding. Also, after 180 min in ^2H_2O, when ~70% of peptide sites are exchanged (Hilton et al., 1981), the combined amide I/amide I′ band is centered at 1658 cm^{-1}. The extensive overlap of amide I and amide I′ markers precludes use of this spectral region for quantitative analysis of peptide exchange kinetics. We therefore turn to the lower-frequency region of the Raman spectrum for suitable markers of peptide NH → N^{2}H exchange.

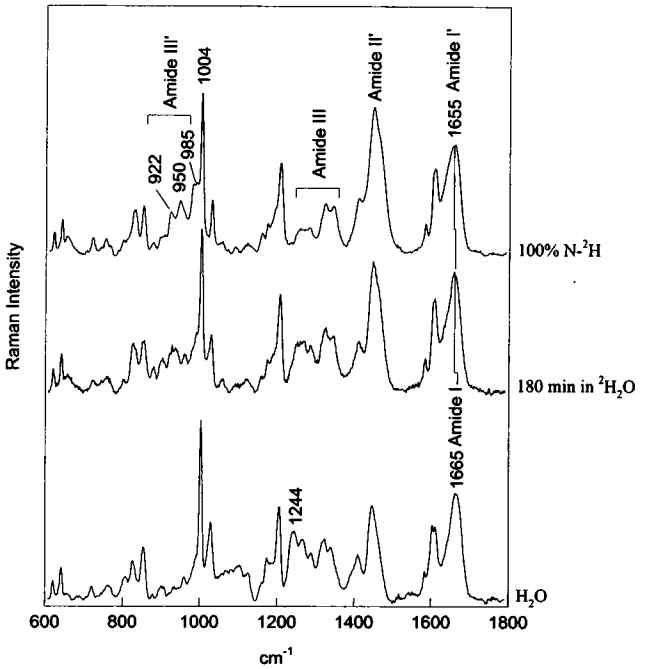

FIGURE 11 Raman spectra (600–1800 cm^{-1}) of fully deuteriated (*top trace*), partially deuteriated (*middle trace*), and protiated (*bottom trace*) forms of BPTI. The top spectrum was collected after unfolding in 0.3 M potassium deuteroxide and refolding in native ^2H_2O buffer, and the middle spectrum after 180 min in ^2H_2O. Labels indicate prominent bands discussed in the text.

Fig. 11 shows that the region 1400–1500 cm^{-1} is highly sensitive to peptide deuteriation. This reflects the occurrence of a new band (assigned as amide II′ by Sugawara et al., 1978), which underlies the prominent methylene and methyl group modes near 1450 cm^{-1}. Oboodi et al. (1984) have rationalized the spectral prominence of the amide II′ mode of deuteriated peptides as a consequence of the decoupling of NH bending and C—N stretching motions. Such decoupling yields the amide II′ vibration as a nearly pure C—N stretching mode; the expected N^{2}H bending component is reflected in the amide III′ mode. Despite overlap with CH_2 and CH_3 deformations, amide II′ can be exploited effectively to monitor exchanges of peptide groups in specific secondary structure domains by Raman spectroscopy (Tuma et al., 1996a). However, the utility of amide II′ difference bands for the present kinetic studies is undermined by interference from the transient ^{2}HOH bending mode that also occurs at 1450 cm^{-1}. Thus, time-resolved Raman spectroscopy of the amide II′ band is effectively limited to examination of relatively slowly exchanging classes of peptide NH groups.

It is clear from Fig. 11 that the intervals of amide III (1200–1300 cm^{-1}) and amide III′ (900–1000 cm^{-1}) modes are most appropriate for monitoring Raman markers of peptide NH and N^{2}H groups, respectively, and accordingly are the best suited to determination of peptide exchange rates. The amide III vibration represents mainly coupled C—N stretching and NH in-plane bending, whereas amide III′ is considered to be largely N^{2}H in-plane bending (Bandekar, 1992). The amide III band of BPTI is very broad and centered at 1244 cm^{-1}. It comprises contributions from peptides in three β-strands and in connecting loops (irregular conformations). On deuteriation, the complex amide III band is replaced by a family of amide III′ bands with identifiable members at ~922, 950, 985 and 990 cm^{-1}. The 922- and 990-cm^{-1} amide III′ markers represent a rapidly exchanging fraction of peptides, which is completely exchanged in less than 180 min (Fig. 11, *middle trace*). We assign the 990-cm^{-1} band to peptides in β-strand secondary structure (Sugawara et al., 1978) and the 922-cm^{-1} band to those in irregular (loop) conformations. On the other hand, the bands at 950 and 985 cm^{-1}, which are relatively sharp, are attributed to α-helices and β-strands in exchange-protected domains. As shown by Fig. 11, the latter are revealed only in the fully deuteriated BPTI molecule. The present assignments are in accord with previous Raman (Sugawara et al., 1978) and NMR (Kim et al., 1993) studies.

The amide III′ region, which is devoid of significant spectral interference, is particularly well suited to quantitative analysis. As a first approximation we assume equal intrinsic intensities for all amide III′ modes. The fraction of exchanged peptide sites in each conformation is then estimated from the corresponding amide III′ band intensity (normalized band area). The resulting time course of normalized integrated difference intensities is shown in Fig. 12. We find that the exchange kinetics are characterized by a fast phase, accounting for ~65% of peptide sites (completed in 60 min), a less rapid phase consisting of ~5% of peptide sites (between 60 and 180 min), and a very slow, or "protected," class consisting of the remaining 30% of peptide sites. The last group constitutes the exchange-protected core (Kim et al., 1993).

The rate of ^2H_2O solvent efflux is the limiting factor in measuring the exchange kinetics of the rapidly exchanging

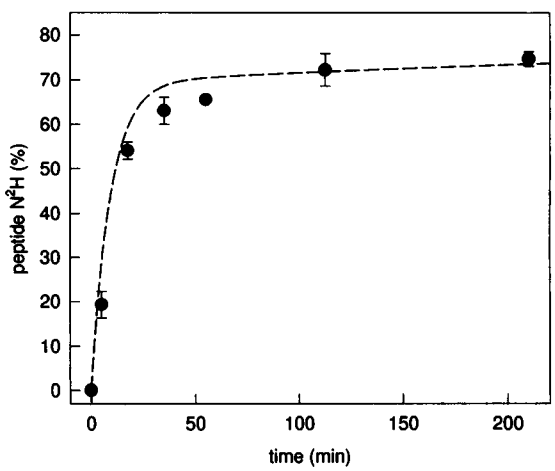

FIGURE 12 Time course of peptide NH → N^{2}H exchange in BPTI at 10°C calculated from the areas of amide III′ band components, as discussed in the text. For comparison, the dashed curve shows the BPTI peptide exchange measured in tritiation analysis by Hilton et al. (1981).

fraction. Peptide sites exchanging on time scales ranging from milliseconds to seconds contribute to this fraction, and these rates are beyond the resolution limit of the present apparatus. However, comparison with previously published results (Hilton et al., 1981; Kim et al., 1993) shows that the observed kinetics and extent of exchange protection are accurately monitored by the Raman method (Fig. 12).

In addition to monitoring deuterium exchange of peptide groups, the present method can be used to characterize deuterium exchange of selected side chains. For example, deuteriation of the tyrosine phenoxyl group is accompanied by a shift of $\sim 6\ cm^{-1}$ in the bands of the Fermi doublet located at 830 and 850 cm^{-1}. Indeed, we observe for BPTI the exchange of a small fraction of tyrosines on a time scale slower than 0.003 min^{-1} (data not shown). This observation can be attributed to exchange of Tyr-35, the phenolic ring of which is interlocked between polar groups (Wlodawer et al., 1987).

In summary, the Raman dynamic probe of NH $\rightarrow$ N^2H exchange in BPTI reveals three kinetic classes of exchangeable sites and identifies the most highly protected sites as those of the β-strand–α-helix core. Recently a similar approach based on monitoring amide II bands in an on-line Fourier-transform infrared (FTIR) rapid mixing experiment was reported (de Jongh et al., 1995). In the FTIR study the authors examined the exchange of two cytochrome *c* variants and compared their results with those obtained in a low-resolution ^{1}H-NMR study. The agreement between solution FTIR and ^{1}H-NMR kinetic analyses was found to be satisfactory. The FTIR and Raman studies demonstrate the effectiveness of vibrational spectroscopy in probing hydrogen-isotope exchange kinetics of aqueous biomolecules.

CONCLUSIONS

We have described the theory, design, and operation of a microdialysis flow cell for investigating isotopic exchanges, chemical titrations, and conformational transitions of macromolecules and their assemblies by time-resolved Raman spectroscopy. We have shown that diffusion theory analysis accounts satisfactorily for the experimental data obtained by the Raman dynamic probe. Rates for efflux of ^2H_2O, H_2O, $Ca(NO_3)_2$, and EGTA were measured, and the rate of pH titration of a biopolymer was determined. Applications of the Raman probe to isotopic hydrogen exchanges of RNA molecules and of the small globular protein BPTI demonstrate the usefulness of the methodology for investigating the structure and dynamics of biological macromolecules. A unique advantage of the time-resolved Raman approach vis-à-vis other spectroscopic methods is its applicability to large assemblies of biological molecules, including viruses and chromosomal complexes.

We thank Prof. Dennis H. Bamford, University of Helsinki, Finland, for the gift of ϕ6 dsRNA and Prof. Clare Woodward, University of Minnesota, St. Paul, for the gift of BPTI. We also thank Dr. James M. Benevides, University of Missouri—Kansas City, for helpful discussions and comments on the manuscript. Support of this research by the U.S. National Institutes of Health (grants GM50776 and GM54378) is gratefully acknowledged.

This paper is Part LV of the series Structural Studies of Viruses by Raman Spectroscopy supported by National Institutes of Health grant GM50776.

REFERENCES

Bamford, J. H. K., D. H. Bamford, T. Li, and G. J. Thomas, Jr. 1993. Structural studies on the enveloped dsRNA bacteriophage ϕ6 of *Pseudomonas syringae* by Raman spectroscopy. II. Nucleocapsid structure and thermostability of the virion, nucleocapsid and polymerase complex. *J. Mol. Biol.* 230:473–482.

Bandekar, J. 1992. Amide modes and protein conformation. *Biochim. Biophys. Acta.* 1120:123–143.

Benevides, J. M., A. H.-J. Wang, A. Rich, Y. Kyogoku, G. A. van der Marel, J. H. van Boom, and G. J. Thomas, Jr. 1986. Raman spectra of single crystals of r(GCG)d(CGC) and d(CCCCGGGG) as models for *A* DNA, their structure transitions in aqueous solution, and comparison with double-helical poly(dG)·poly(dC). *Biochemistry.* 25:41–50.

Caillé, J.-P., M. Pigeon-Gosselin, and M. Pézolet. 1983. Laser Raman study of internally perfused muscle fibers: effect of Mg^{2+}, ATP and Ca^{2+}. *Biochim. Biophys. Acta.* 758:121–127.

Connelly, G. P., Y. Bai, M.-F. Jeng, and S. W. Englander. 1993. Isotope effect in peptide group hydrogen exchange. *Proteins.* 17:87–92.

de Jongh, H. H. J., E. Goormaghtigh, and J-M. Ruysschaert. 1995. Tertiary stability of native and methionine-80 modified cytochrome *c* detected by proton-deuterium exchange using on-line Fourier transform infrared spectroscopy. *Biochemistry.* 34:172–179.

Englander, J. J., D. B. Calhoun, and S. W. Englander. 1979. Measurement and calibration of peptide group hydrogen-deuterium exchange by ultraviolet spectrophotometry. *Anal. Biochem.* 92:517–524.

Englander, S. W., and N. R. Kallenbach. 1984. Hydrogen exchange and structural dynamics of proteins and nucleic acids. *Q. Rev. Biophys.* 16:521–655.

Guéron, M., and J.-L. Leroy. 1992. Base-pair opening in double-stranded nucleic acids. *In* Nucleic Acids and Molecular Biology, Vol. 6. F. Eckstein and D. M. J. Lilley, editors. Springer-Verlag, Berlin.

Hester, R. E. 1987. Raman spectroscopic studies of transient chemical species. *In* Time-Resolved Laser Raman spectroscopy. D. Phillips and G. H. Atkinson, editors. Harwood Academic Publishers, New York. 4–22.

Hilton, B. D., K. Trudeau, and C. K. Woodward. 1981. Hydrogen exchange rates in pancreatic trypsin inhibitor are not correlated to thermal stability in urea. *Biochemistry.* 20:4697–4703.

Jacrot, B. 1975. Studies on assembly of a spherical plant virus. II. The mechanism of protein aggregation and virus swelling. *J. Mol. Biol.* 95:433–446.

Kim, K-S., J. A. Fuchs, and C. K. Woodward. 1993. Hydrogen exchange identifies native-state motional domains important in protein folding. *Biochemistry.* 32:9600–9608.

Koenig, J. L., and B. Frushour. 1972. Raman studies of the helix-to-coil transition in poly-L-glutamic acid and poly-L-ornithine. *Biopolymers.* 11:1871–1892.

Li, T. 1992. Investigation of molecular recognition by static and dynamic methods of Raman spectroscopy: applications to RNA plant viruses and DNA-protein complexes. Ph.D. dissertation. University of Missouri, Kansas City.

Li, T., J. E. Johnson, and G. J. Thomas, Jr. 1993. Raman dynamic probe of hydrogen exchange in bean pod mottle virus: base specific retardation of exchange in packaged ssRNA. *Biophys. J.* 65:1963–1972.

Lord, R. C., and N.-T. Yu. 1970. Laser-excited Raman spectroscopy of biomolecules II. Native ribonuclease and α-chymotrypsin. *J. Mol. Biol.* 51:203–213.

Mandal, C., N. R. Kallenbach, and S. W. Englander. 1979. Base-pair opening and closing reactions in the double helix. A stopped-flow hydrogen exchange study in poly(rA)·poly(rU). *J. Mol. Biol.* 135: 391–411.

Miura, T., and G. J. Thomas, Jr. 1995a. Structure and dynamics of interstrand guanine association in quadruplex telomeric DNA. *Biochemistry.* 34:9645–9653.

Miura, T., and G. J. Thomas, Jr. 1995b. Raman spectroscopy of proteins and their assemblies. *In* Subcellular Biochemistr, Vol. 24. B. B. Biswas and S. Roy, editors. Plenum Publishing Company, New York. 55–99.

Oboodi, M. R., C. Alva, and M. Diem. 1984. Solution phase Raman studies of alanyl dipeptides and various isotopomers: a reevaluation of the amide III vibrational assignment. *J. Phys. Chem.* 88:501–505.

Olkkonen, V. M., P. Gottlieb, J. Strassman, X. Qiao, D. H. Bamford, and L. Mindich. 1990. In vitro assembly of infectious nucleocapsids of bacteriophage $\phi 6$: formation of a recombinant double-stranded RNA virus. *Proc. Natl. Acad. Sci. USA.* 87:9173–9177.

Orlova, A., and E. H. Egelman. 1995. Structural dynamics of F-actin. I. Changes in the C-terminus. *J. Mol. Biol.* 245:582–597.

Ozisik, M. N. 1980. Heat Conduction. John Wiley & Son, New York.

Prevelige, P. E., Jr., D. Thomas, K. L. Aubrey, S. A. Towse, and G. J. Thomas, Jr. 1993. Subunit conformational changes accompanying bacteriophage P22 capsid maturation. *Biochemistry.* 32:537–543.

Reilly, K. E., and G. J. Thomas, Jr. 1994. Hydrogen exchange dynamics of the P22 virion determined by time-resolved Raman spectroscopy. *J. Mol. Biol.* 241:68–82.

Saenger, W. 1984. Principles of Nucleic Acid Structure. Springer-Verlag, New York.

Speir, J. A., S. Munshi, G. Wang, T. S. Baker, and J. E. Johnson. 1995. Structures of the native and swollen forms of cowpea chlorotic mottle virus determined by x-ray crystallography and cryo-electron microscopy. *Structure.* 3:63–78.

Sugawara, J., I. Harada, H. Matsuura, and T. Shimanouchi. 1978. Preresonance Raman studies of poly(L-lysine), poly(L-glutamic acid) and deuterated *N*-methylacedamides. *Biopolymers.* 17:1405–1421.

Teitelbaum, H., and S. W. Englander. 1975. Open states in native polynucleotides. I. Hydrogen-exchange study of adenine-containing double helices. *J. Mol. Biol.* 92:55–78.

Teschke, C. M., and J. King. 1993. Folding of the phage P22 coat protein in vitro. *Biochemistry.* 32:10839–10847.

Thomas, G. J., Jr., and J. Barylski. 1970. Thermostating capillary cells for a laser Raman spectrometer. *Appl. Spectrosc.* 24:463–464.

Thomas, G. J., Jr., and K. A. Hartman. 1973. Raman studies of nucleic acids VIII. Estimation of RNA secondary structure from Raman scattering by phosphate group vibrations. *Biochim. Biophys. Acta.* 312: 311–322.

Thomas, G. J., Jr., and M. Tsuboi. 1993. Raman spectroscopy of nucleic acids and their complexes. *Adv. Biophys. Chem.* 3:1–70.

Tuma, R., J. H. K. Bamford, D. H. Bamford, M. P. Russell, and G. J. Thomas, Jr. 1996a. Structure, interactions and dynamics of PRD1 virus. I. Coupling of subunit folding and capsid assembly. *J. Mol. Biol.* 257:87–101.

Tuma, R., J. H. K. Bamford, D. H. Bamford, and G. J. Thomas, Jr. 1996b. Structure, interactions and dynamics of PRD1 virus. II. Organization of the viral membrane and DNA. *J. Mol. Biol.* 257:102–115.

Weast, R. C., and S. M. Selby, editors. 1966. CRC Handbook of Chemistry and Physics, 47th ed. CRC Press, Cleveland, OH. F43–F44.

Wlodawer, A., J. Deisenhofer, and R. Huber 1987. Comparison of two highly refined structures of bovine pancreatic trypsin inhibitor. *J. Mol. Biol.* 193:145–156.